Molecular basis of HACD-TECR complex mediated very-long-chain fatty acid elongation reveal a potential target in colorectal cancer

Rui Lv[1,2,#], Leiye Yu[1,3,#], Jingyi Liu[2,4,#], Youli Zhou[5,6,#], Ruiping He[1,#], Chen Wang[1], Bing Gan[1], Rujuan Ti[7], Haizhan Jiao[5], Baohui Song[4], Yiqi Chen[1], Feifei Lin[8], Mei Gao[6], Hongli Hu[5], Shankai Yin[3], Pinghong Zhou[4], Lizhe Zhu[7], Mingyan Cai[4], Tian Xie[9,*], Jia Liu[8,*], Li Chen[1,10,*], Yunshi Zhong[2,4,*], Ruobing Ren[1,2,*]

[1] Shanghai Key Laboratory of Metabolic Remodeling and Health, Institute of Metabolism and Integrative Biology, Fudan University, Shanghai 200437, China

[2] Shanghai Xuhui Central Hospital, Zhongshan-Xuhui Hospital, Fudan University, Shanghai 200020, China

[3] Department of Otorhinolaryngology Head and Neck Surgery, Shanghai Sixth People's Hospital Affiliated to Shanghai Jiao Tong University School of Medicine, Shanghai 200233, China

[4] Endoscopy Center and Endoscopy Research Institute, Zhongshan Hospital, Fudan University, Shanghai 200032, China

[5] Kobilka Institute of Innovative Drug Discovery, School of Medicine, The Chinese University of Hong Kong, Shenzhen, Guangdong 518172, China

[6] Central Research Laboratories, Chongqing General Hospital, Chongqing University & Chongqing Academy of Medical Sciences, 118 Xingguang Avenue, Liangjiang New Area, Chongqing 401147, China

[7] Warshel Institute of Computational Biology, School of Medicine, The Chinese University of Hong Kong, Shenzhen, Guangdong 518172, China

[8] China-Serbia "Belt and Road" Joint Laboratory for Natural Products and Drug Discovery, Shanghai Institute of Materia Medica, Chinese Academy of Sciences, 555 Zuchongzhi Road, Zhangjiang Hitech Park, Shanghai 201203, China

[9] MOE Key Laboratory of Geriatric Diseases and Immunology, Biomedical Basic Research Center of Jiangsu, Institute of Molecular Enzymology, School of Life Sciences, Suzhou Medical College of Soochow University, Suzhou, Jiangsu, 215123, China

[10] Obstetrics and Gynecology Hospital, Fudan University, Shanghai 200438, China

[#] These authors contributed equally

* To whom correspondence should be addressed. Email: renruobing@fudan.edu.cn

Abstract

Very long-chain fatty acids (VLCFAs) are crucial for lipid homeostasis and physiological functions. The elongation of VLCFAs, which is mediated by four consecutive enzymes in the endoplasmic reticulum (ER), has been implicated in tumor progression. However, the molecular mechanisms underlying VLCFA elongation enzymes and their specific contributions to tumorigenesis remain largely elusive. Here, we demonstrate that trans-2-enoyl-CoA reductase (TECR) is upregulated in colorectal cancer (CRC). Structural and biochemical analyses revealed a conserved catalytic mechanism for TECR-mediated trans-2-enoyl-CoA reduction. Moreover, we show that TECR forms a stable complex with 3-hydroxyacyl-CoA dehydratase (HACD), to cooperatively drive VLCFA elongation. A unique U-shaped loop in HACD is critical for recognizing TECR. Disruption of the HACD–TECR interaction interface significantly suppresses CRC cell growth. Collectively, these findings elucidate the molecular mechanism of HACD–TECR-mediated VLCFA elongation and suggest a potential therapeutic strategy for CRC treatment by modulating VLCFA metabolism.

Introduction

Very long-chain fatty acids (VLCFAs) are fatty acids with carbon chains of 20 or more, serving as structural components of membrane lipids and participating in membrane dynamics, lipid metabolism, and cell signal transduction[1-4]. Dysfunction in the VLCFA elongation process has been linked to cancers, cardiovascular diseases, musculoskeletal disorders, and neurological degenerations[5, 6]. The biosynthesis of VLCFAs occurs in the endoplasmic reticulum (ER) through a four-step elongation cycle, mediated by four membrane-bound enzymes[1, 7]. The Elongation of Very Long-Chain Fatty Acids (ELOVL) enzyme family (ELOVL1–7 in humans) catalyzes the first and rate-limiting step by condensing acyl-CoA with malonyl-CoA to form 3-ketoacyl-CoA[7], which is then reduced to 3-hydroxyacyl-CoA by 3-ketoacyl-CoA reductase (KAR)[8]. The 3-Hydroxyacyl-CoA Dehydratase (HACD) enzyme family (HACD1–4 in humans) converts this intermediate to trans-2-enoyl-CoA[9], which is subsequently reduced by trans-2,3-enoyl-CoA reductase (TECR) to generate an elongated acyl-CoA with two additional carbon units[8] (Fig. 1a).

For efficient VLCFA biosynthesis, these components function in a coordinated manner, facilitated by protein–protein interactions and potential feedback regulatory mechanisms[9-15]. Notably, sub-complexes such as ELOVL-KAR and HACD-TECR have been identified and shown to modulate enzymatic activities[12, 14-17]. These findings support a model of coordinated action among the components of the human VLCFA elongation complex. However, the detailed molecular mechanisms underlying the function of the VLCFA elongation holoenzyme and its subcomplexes remain poorly understood.

Lipid metabolic reprogramming is a hallmark of tumor progression[18-28]. Recent studies have demonstrated that ELOVL enzymes are implicated in the development of several cancers, including

prostate cancer, breast cancer, colorectal cancer, and lung cancer[21, 24-26]. Silencing TECR also inhibits tumor cell proliferation and colony formation in breast cancer cell lines[27]. Thus, modulation of VLCFA synthesis holds therapeutic potential for targeted cancer treatments[23, 25], and understanding the molecular mechanisms underlying VLCFA elongation may offer valuable insights. While ELOVLs vary in tissue distribution and substrate specificity, other enzymes exhibit broader substrate preferences. As the sole enzyme catalyzing the final step of the VLCFA elongation cycle, TECR is essential for completing this biochemical reaction. Given that TECR is the only isoform present in humans, targeting TECR to modulate VLCFA elongation presents a rational and potentially effective therapeutic strategy.

In this study, we demonstrated that TECR is enriched in colorectal cancer (CRC) cells through bioinformatic analysis. We also established an in vitro enzymatic system to characterize the functional role of TECR in VLCFA elongation. We then determined the high-resolution three-dimensional structure of the HACD–TECR complex, deciphering the catalytic mechanisms of the dehydration and reduction steps, and revealing a cooperative interaction between HACD and TECR. Furthermore, we demonstrated that disrupting either the enzyme activity of TECR or the HACD–TECR interface significantly suppressed CRC cell proliferation, highlighting its potential for designing orthosteric or allosteric modulators as therapeutic agents, offering promising new treatment avenues.

Results

TECR is enriched in human CRC

To investigate the association between TECR and tumorigenesis across cancer types, we performed bioinformatics analysis using The Cancer Genome Atlas (TCGA) database to evaluate TECR expression. The results revealed significant upregulation of TECR in tumors, including breast, ovarian, and colorectal cancers (CRC) compared to normal tissues (Fig. S1a). Given its overexpression in tumors, we further examined the role of TECR in tumorigenesis by conducting Cell Counting Kit-8 (CCK-8) cell proliferation assays. It showed that TECR silencing markedly suppressed the proliferation of CRC cell lines such as HCT116, SW480, and SW620, compared to other cancer cell types (Fig. 1b, c, S2).

Further analysis of the Gene Expression Omnibus (GEO) dataset (GSE184093)[29] confirmed that TECR is significantly upregulated in CRC samples at the transcriptome level (Fig. 1d). Consistently, the Clinical Proteomic Tumor Analysis Consortium (CPTAC) data showed increased TECR protein expression in CRC tissues (Fig. 1e). Single-cell RNA sequencing data from a CRC cohort (GSE132465)[30] revealed TECR enrichment in epithelial cells, particularly in primary tumor cells compared to normal epithelium (Fig. S1b-d). Additionally, we performed Immunohistochemistry (IHC) of a tissue microarray with 87 paired CRC samples (carcinoma, adenoma, and adjacent normal tissues) demonstrating marked TECR overexpression (Fig. 1f and g). Upregulation was observed at the adenoma stage, suggesting its role in early colorectal tumorigenesis. These findings collectively indicate TECR's involvement in CRC development and progression.

In vitro reconstitution of the VLCFA elongation process

To elucidate the molecular function of TECR, which catalyzes the final reduction step in the VLCFA elongation cycle by reducing trans-2-enoyl-CoA (Fig. 1a), we developed a liquid chromatography-mass

spectrometry (LC-MS) based biochemical assay. Mammalian cells express seven ELOVL and four HACD isoforms, and characterizing individual isoforms using cell membrane–based in vitro elongation assays has proven challenging[10]. We reconstituted the VLCFA elongation complex in solution, including ELOVLs, KAR, HACDs, and TECR (Fig. 2a). Given the substrate selectivity of ELOVLs and the known interaction between HACD and TECR, we selected human ELOVL3 and HACD2 as representative isoforms for reconstitution. Recombinantly expressed ELOVL3, KAR, and the HACD2-TECR subcomplex were individually purified and subsequently assembled into the VLCFA elongation complex (Fig. 2a). To differentiate LC-MS signals from products and endogenous lipids co-purified with membrane-associated VLCFA enzymes, we introduced ^{12}C18:0 acyl-CoA and ^{13}C-Malonyl-CoA substrates into the complex (Fig. 2b). The elongated acyl-CoA product was subjected to saponification before non-targeted LC-MS analysis for direct detection and quantification. As expected, the fatty acid (FA) species with 20- and 22-C alkyl-chains bearing ^{13}C atoms were robustly detected (Fig. 2c-e). In contrast, replacing wild-type (WT) ELOVL3 with the catalytically inactive H148A mutant completely abolished elongation activity (Fig. 2d, e). This assay offers a superior alternative by providing an exceptionally clean background, high reproducibility, and adaptability for evaluating the activity of diverse combinatorial assemblies of VLCFA elongation enzymes and their mutants.

An attempt to determine the human HACD2-TECR complex structure

To understand the structural basis for TECR function in VLCFA elongation, we aimed to determine the atomic structures of human TECR alone and in complex with other elongation enzymes using cryo-EM. With a molecular weight of 36 kDa, TECR alone presents challenges for cryo-EM studies. Although it is hypothesized that VLCFA elongation enzymes may form a mega-complex for efficient catalysis and regulation, attempts to reconstitute the entire complex were unsuccessful. Our previous study

127 demonstrated that human HACD1/2 and TECR form a stable subcomplex *in vitro*[12]. Other studies also
128 suggest that VLCFA elongation enzymes might achieve synergistic catalysis through physical
129 interactions by forming sub-complexes[14, 17]. Given the high sequence similarity and functional
130 redundancy between HACD1 and HACD2, we selected the HACD2 isoform for co-assembly with TECR
131 for further structural and functional analyses.

132 The mammalian cell co-expressed HACD2-TECR complex was purified via affinity chromatography and
133 exhibited monodisperse behavior on size exclusion chromatography (Fig. S3a). Despite numerous
134 attempts, we were unable to obtain a high-resolution map of the human HACD2-TECR complex (Fig.
135 S3b-c). To enhance complex stability for structural studies, we crosslinked the complex using
136 glutaraldehyde, and achieved a final 3D map with an overall resolution of 6.32 Å (Fig. S4a-e, Table S1).
137 AlphaFold-predicted models of HACD2 and TECR were fitted into the EM map and manually adjusted
138 (Fig. S4f). Both proteins contain six transmembrane helices, and their TM3/6 regions pack against each
139 other. TECR also possesses an extra N-terminal ubiquitin-like domain. However, the moderate
140 resolution of human HACD2-TECR complex was insufficient to assign side chains of most residues,
141 limiting our understanding of catalytic mechanisms and potential cooperative interactions.

142 **Cryo-EM structure of the CeHACD-CeTECR complex**

143 To elucidate the precise molecular mechanism of HACD-TECR, we screened conserved homologs of
144 human HACDs and TECRs from various species for cryo-EM studies. After extensive screening, we
145 identified the *Caenorhabditis elegans (C. elegans)* HACD-TECR (CeHACD-CeTECR) sub-complex,
146 which behaved good in solution (Fig. S5a). *C. elegans* possesses a highly conserved VLCFA elongation
147 system, with CeHACD and CeTECR sharing 47% and 53% sequence similarity with human HACD2 and

TECR, respectively (Fig. S6, 7). Following comprehensive cryo-EM investigations on the CeHACD-CeTECR complex, we obtained a final 3D reconstruction map with an overall resolution of 3.6 Å (Fig. S5b-f, Table S1).

The well-defined electron density enabled accurate modeling of the CeHACD-CeTECR complex (Fig. S5g). Similar to human HACD2 and TECR, both CeHACD and CeTECR contain six transmembrane helices, with CeTECR also featuring an additional N-terminal ubiquitin-like domain (Fig. 3a, Fig. S6, 7). Three intriguing structural features emerged from the high-resolution structure: first, both HACD and TECR exhibit a central cavity that opens towards the cytosolic side of the membrane, with positively charged regions potentially facilitating binding with acyl-CoA substrates (Fig. 3b). Second, both HACD and TECR possess a lateral cleft facing each other, formed by TM3/6 of HACD and TECR, respectively, suggesting a substrate translocation pathway for coordinating sequential dehydration and reduction reactions (Fig. 3b, c). Third, the loop region connecting TM5/6 of HACD interacts with the loop regions connecting TM3/4 and TM5/6 of TECR at the luminal leaflet to stabilize the HACD-TECR complex (Fig. 3a, d). Details of the HACD-TECR interface will be discussed later.

Superposition of human and worm HACD-TECR models revealed similar assembly, with minor shifts in subunits or domains (Fig. S8a-d). Specifically, the structures of HACD proteins, TECR transmembrane regions, and TECR ubiquitin-like domains are highly conserved, with root-mean-square deviations (RMSDs) of 1.806 Å, 1.654 Å, and 1.166 Å among 187, 154, and 67 $C\alpha$ atoms, respectively (Fig. S8b-d). Both human and worm HACD-TECR complexes exhibit two central cavities with positively charged regions and opposing lateral clefts for substrate translocation (Fig. 3b-c, S8e-f). Likewise, the human HACD2 and TECR subunits are held together by the TM5/6 loop region of HACD2 and TM3/4 loop and TM5/6 loop regions of TECR (Fig. S8g). The interface between HACD2 and TECR may be crucial for

protein folding and function, as the purified HACD2 or TECR alone exhibited poor behavior in SEC (Fig. S8h).

TECR possesses a conserved reduction mechanism

TECR belongs to the 5-alpha reductases family. Dali search analysis showed that the structure of TECR closely resembles that of steroid 5-alpha reductases (SRD5As), with an RMSD of 1.996 Å among 169 Cα atoms between CeTECR and human SRD5A2 (HsSRD5A2) (Fig. S9a). The SRD5As contain seven transmembrane helices, with TM1/2/4/7 and TM3/5/6/7 responsible for binding steroid substrate and NADPH reductant, respectively[31, 32]. Compared to the transmembrane domain (TMD) of TECR, the TMD of SRD5A includes an additional transmembrane helix, designated as TM1, positioned outside the central TM2-7 region (Fig. S9a). Previous studies suggest TM1 in SRD5A facilitates substrate entry and release. Given that steroid substrates are smaller, more hydrophobic and rigid than the very long-chain trans-enoyl CoA, SRD5A likely uses TM1 as a gate to regulate their entry and release (Fig. S9a, b). In contrast, TECR's lack of this helix, providing greater spatial accommodation for the larger, amphiphilic, and more flexible very long-chain trans-enoyl CoA substrates between TM3 and TM6 (Fig. S9a, b). Notably, Superposition of SRD5A2 with the CeHACD-CeTECR complex reveals that TM1 of SRD5A2 is located between the transmembrane regions of HACD and TECR, obstructing potential substrate translocation pathways (Fig. S9c). Overall, TECR’s lack of this N-terminal helix ensures effective catalysis of larger substrates and facilitates substrate translocation.

5-alpha reductases family enzymes reduce double bonds in lipid substrates in an NADPH-dependent manner[31, 32]. An omit electron density within the cavity of CeTECR facing the cytoplasm was identified and corresponded well with an NADPH molecule, which was coordinated by polar residues such as

R141, R150, R219, Y248, E251, K285, and Y289, in the TM2/4/5/6 and adjacent loop regions of TECR through numerous hydrogen bonds (Fig. 4a-c). Structural comparisons revealed that both TECR and SRD5A2 share similar NADPH-coordination residues, with aligned transmembrane regions responsible for substrate and NADPH binding, suggesting the conserved catalytic mechanisms (Fig. S9a, d).

Prior studies on HsSRD5A2 have demonstrated that residues E57 and Y91 form hydrogen bonds with the ketone group at C3 position of the steroid substrate, stabilizing the carbonyl group and aligning its C4-C5 double bond with the reactive nicotinamide moiety of NADPH, and facilitating hydride-ion transfer from NADPH to steroid substrates[31, 32]. Sequence alignments and structural comparisons between SRD5A2 and TECR revealed that while NADPH and the catalytic tyrosine (Y138 in CeTECR; Y138 in HsTECR; Y91 in HsSRD5A2) are in similar positions, the catalytic glutamate in TECR (E95 in CeTECR; E94 in HsTECR) is shifted by one amino acid relative to E57 in HsSRD5A2 (Fig. 4d, S7, S9e). In HsSRD5A2, the distance between E57 and Y91 is 5 Å, allowing coordination of the C3 carbonyl group, whereas in TECR, the 9.3 Å distance between E95 and Y138 prevents simultaneous coordination of the carbonyl group in trans-2-enoyl-CoA (Fig. 4d). Further analysis of residues near the catalytic glutamate and NADPH cofactor revealed two tyrosines (Y96 and Y168 in CeTECR; Y95 and Y168 in HsTECR) positioned within 6 Å of the glutamate residue, oriented toward the catalytic pocket (Fig. 4d-e, S9e). We hypothesized that these two tyrosines, instead of Y138, may cooperate with the glutamate residue to coordinate the carbonyl group of the trans-2-enoyl-CoA substrate.

Based on the analysis, we conducted mutagenesis experiments on HsTECR, confirming that the E94L mutation reduced activity by 70% during one elongation cycle and abolished further elongation (Fig. 4f). The Y95F mutation reduced activity by 35% during one cycle and 80% over two cycles, while the Y168F reduced activity by 60% during one cycle and abolished further elongation (Fig. 4f). In contrast, the

Y138F mutation had no effect (Fig. 4f). Collectively, we propose that in human TECR, E94 collaborates with Y95 or Y168 to coordinate the carbonyl oxygen of trans-2-enoyl-CoA, thereby positioning the adjacent C2-C3 double bond in close proximity to NADPH for hydride transfer (Fig. 4g). Despite the shifted catalytic residues, TECR and SRD5A employ a conserved reductive mechanism. The subtle shift in the positions of catalytic residues may have evolved to optimize substrate specificity within the reductase family. Due to the lack of a substrate-bound TECR structure, further investigations are needed to precisely identify the binding site for trans-enoyl-CoA.

TECR deficiency impairs VLCFA synthesis in CRC cells and suppresses tumorigenesis

To investigate the functional role of TECR in colorectal cancer (CRC), we stably knocked down TECR expression in HCT116 and SW480 cell lines using short hairpin RNA (shRNA). Consistent with transient siRNA knockdown, stable TECR knockdown inhibited CRC cell proliferation (Fig. 5a-c). Additionally, flow cytometric analysis showed that TECR knockdown induced S-phase arrest in HCT116 and SW480 cells (Fig. S10a). The trans-well assay also showed suppress of migratory and invasive capacities of HCT116 and SW480 cell lines (Fig. S10b). Collectively, *in vitro* studies demonstrated that knockdown of TECR substantially suppresses the progression of CRC.

Since TECR plays crucial role in VLCFA elongation, we performed saponification and total fatty acid analysis of HCT116 cells by LC-MS. Lipidomic analysis revealed that TECR knockout significantly reduced cellular VLCFA levels (Fig. 5d). To further confirm the VLCFA-dependent CRC growth manner, we cultured HCT116 cells in delipidated fetal bovine serum (DFBS) medium. Supplementation with VLCFAs (22:0–26:0) rescued TECR-KD cell growth, whereas supplementation with long-chain fatty acids (16:0–18:0) had no effect (Fig. 5e). To exclude the effect of non-enzyme function of TECR, we

expressed catalytically defective human TECR mutants in TECR-KD cells and failed to rescue the growth defect (Fig. 5f, g). These results confirm the importance of TECR's enzymatic activity in CRC proliferation.

Furthermore, we generated subcutaneous xenograft tumor models by injecting BALB/c nude mice with either shTECR-transduced or conventional HCT116 cells. The shTECR group showed significantly slower tumor growth compared to the control group (Fig. 5h). Tumors derived from shTECR-HCT116 cells also exhibited a markedly lower weight and smaller volume (Fig. 5i). Immunofluorescence staining of tumor samples showed that Ki-67 expression was reduced in TECR-deficient tumors, confirming a suppression of CRC cell proliferation (Fig. S10c, d). In conclusion, these results highlight the crucial role of TECR in promoting CRC cell proliferation both *in vitro* and *in vivo*.

Cooperative mechanism between HACD and TECR

HACD catalyzes the dehydration step in the VLCFA elongation cycle, converting 3-hydroxyacyl-CoA to trans-2-enoyl-CoA (Fig. 1a). This product is then immediately reduced by TECR to yield an elongated acyl-CoA. The structure of HACD comprises six transmembrane helices that form a central cavity suitable for substrate binding and catalysis (Fig. 3b, 6a, S8e). A Dali search revealed structural similarity between HACD and human ELOVL7, which catalyzes the first condensation reaction [33](Fig. 1a). Structural comparison revealed that TM1-6 of HACD resemble TM2-7 of ELOVL7, with an RMSD of 4.445 Å between 97 Cα atoms (Fig. S11a). Both enzymes have an occluded cavity for substrate binding and catalysis (Fig. S11a, b). Despite similar structural folds, HACD and ELOVL catalyze different reactions—dehydration and condensation, respectively—suggesting they share similar binding pockets for acyl-CoA substrates but have evolved distinct catalytic residues.

To elucidate the potential substrate binding and catalytic mechanisms of HACD, we employed molecular dynamics (MD) simulations to dock C18:0 3-hydroxyacyl-CoA substrate into CeHACD. The docking analysis revealed that the acyl-CoA substrate occupies a position similar to that observed in ELOVL7, particularly regarding the CoA moiety (Fig. S11c). To identify potential catalytic residues in HACD, we analyzed polar residues positioned near the C-2 and C-3 atoms of the 3-hydroxyacyl chain, the sites of the dehydration reaction. MD simulations showed that the highly conserved polar residues Y142 and E149 in TM5 of CeHACD remain in close proximity to the C-2 and C-3 positions of the 3-hydroxyacyl-CoA substrate throughout the simulation (Fig. 6b, S6, S11d).

To validate their roles, we generated the equivalent HsHACD2 mutants, Y176A and E183A, and measured the enzymatic activities. The Y176A mutation reduced activity by 80% during one elongation cycle and abolished subsequent cycles, while the E183A mutation nearly completely lost activity (Fig. 6c). A previous study on yeast PHS1, a homolog of HACD, showed that the equivalent residues Y149 and E156 are essential for activity[34]. These results collectively highlight the critical roles of these conserved residues. Based on structural and biochemical analyses, we propose a catalytic mechanism for HACD, where the tyrosine residue abstracts a proton from the C-2 position, and the glutamate residue facilitates the elimination of the hydroxyl group at C-3, mediating the dehydration step in fatty acid elongation (Fig. S11e).

The translocation of the product generated by HACD towards TECR as a substrate may be facilitated by the interaction between HACD and TECR, primarily mediated by the TM5/6 loop of HACD and TM3/4 and TM5/6 loops of TECR at the luminal leaflet (Fig. 3d, S8g). Compared to the TM6/7 helices in ELOVL7, the formation of HACD-TECR complex induces a shift and rotation of TM5/6 helices in HACD, with the exterior portion displaced by approximately 15 Å towards TECR (Fig. S11f). This movement

277 positions the product generated by HACD closer to the putative substrate entry site in TECR formed by
278 TM3 and TM6 (Fig. S11f). Thus, we hypothesize that the adhesive interactions between the loop regions
279 of HACD and TECR promote close spatial apposition, enhance functional coordination, and improve
280 catalytic efficiency by facilitating product transfer from HACD to TECR.

281 **Disruption of the HACD-TECR complex interface inhibits CRC cell growth**

282 The TM5/6 loop of HACD adopts a unique U-shaped conformation, stabilized by five intra-loop hydrogen
283 bonds. Specifically, N172 forms three hydrogen bonds with E169, L174, and M176, while L168 and I178
284 form two additional hydrogen bonds (Fig. 6d). The HACD-TECR interface is stabilized by four
285 intermolecular hydrogen bonds. Notably, the side chain of N175 forms two hydrogen bonds with the
286 main chains of T185 and Q263 in TECR, whereas the main chains of N172 and R173 form two other
287 hydrogen bonds with the side chains of T185 and Q263, respectively (Fig. 6d). Besides, M170 and N175
288 residues of HACD insert into a small cavity formed by the TM3/4 and TM5/6 loops of TECR (Fig. 6e).
289 While N175 is coordinated by polar interactions with T185 and Q263 of TECR, the M170 residue is
290 stabilized by hydrophobic interactions with F178 and L183 of TECR (Fig. 6e). Sequence alignments
291 indicate that the key residues involved in intra-loop and inter-loop interactions, particularly those
292 contributing side-chain contacts, are highly conserved between worm and human (Fig. S6, 7),
293 suggesting that the molecular interactions mediating HACD-TECR complex formation are evolutionarily
294 conserved.

295 We performed co-immunoprecipitation (co-IP) assays to assess the functional role of residues at the
296 HACD-TECR interface. The CeHACD-N172A mutation completely abolished binding between CeHACD
297 and CeTECR (Fig. 6f), indicating that the U-shaped conformation of the TM5/6 loop is crucial for

298 interaction with CeTECR. Similarly, mutations disrupting intermolecular polar interactions (CeHACD-
299 N175A, CeTECR-T185P, CeTECR-Q263P) prevented complex formation (Fig. 6f). The CeHACD-
300 M170A mutation, which disrupts hydrophobic interactions, also abrogated the CeHACD-CeTECR
301 interaction (Fig. 6f). Equivalent mutations in HsHACD2 and HsTECR (L204A, N206A, N209A, T185P,
302 Q263P) impaired complex formation similarly (Fig. 6g, S6, S7). These results highlight the essential
303 roles of conserved intra-loop and inter-loop interactions in stabilizing the HACD-TECR complex.

304 To investigate the functional relevance of the HACD-TECR interface in CRC cells, we expressed the
305 interface-disrupting HsTECR-T185P and HsTECR-Q263P mutants in TECR-KD HCT116 cells. While
306 expression of WT HsTECR fully restored HCT116 cell growth, both the HsTECR-T185P mutant and the
307 HsTECR-Q263P mutant rescued only about 40% of tumor cell proliferation compared to WT HsTECR
308 (Fig. 6h, i). These results indicate that disrupting the HACD-TECR interface effectively suppresses tumor
309 cell proliferation.

310 Discussion

311 Given the importance of VLCFA biosynthesis pathway in various cancers, understanding the molecular
312 mechanisms of the VLCFA elongation complex and its subcomplexes is crucial for therapeutic
313 development. In this study, we uncovered the molecular mechanisms of TECR and HACD functions,
314 and identified the specific interface between HACD and TECR, suggesting a potential cooperative
315 mechanism between these two enzymes. We found that TECR is highly expressed in CRC patients,
316 and TECR knockdown significantly suppresses CRC tumor growth and cell proliferation. Besides,
317 disruption of the HACD-TECR interface also inhibited CRC cell growth. Thus, two distinct strategies
318 targeting TECR to modulate VLCFA biosynthesis have emerged.

Firstly, considering TECR as an NADPH-dependent reductase, an orthosteric inhibitor represents a conventional approach (Fig. 7a). The success of inhibitors targeting SRD5A2 gives us confidence in this strategy. Finasteride and dutasteride, approved for the treatment of alopecia and benign prostate enlargement, effectively inhibit SRD5A2 activity[35-37]. The catalytic residue E57 of SRD5A2 facilitates hydride transfer from NADPH to the Δ1,2 bond of finasteride and dutasteride, resulting in enolization and the formation of a covalent NADP-DHF intermediate. A similar strategy may be applied to the design of TECR orthosteric inhibitor. However, the lack of a substrate-bound structure and detailed interaction data hinders structure-based rational design. It is worth noting that inhibiting TECR may lead to the accumulation of trans-2-enoyl-CoA, its substrate. A previous study on ELOVL7 proposed a side reaction with trans-2-enoyl-CoA as an abnormal ELOVL substrate, resulting in irreversible inhibition[33]. Therefore, a TECR inhibitor could potentially cause a dual inhibition effect on both TECR and ELOVL7 in cells.

Secondly, we emphasize the physiological importance of specific interaction between HACD and TECR in VLCFA elongation. Compromising the complex may lead to the release of the intermediate trans-2-enoyl-CoA by HACD into the ER membrane environment, where it could either be degraded through beta-oxidation or covalently link into ELOVLs[33], lowering catalytic efficiency. Thus, an allosteric modulator that disrupts the complex formation represents a brand-new approach for therapeutics development (Fig. 7b). Leveraging our defined structural interface between HACD and TECR, we established a peptide competition assay to screen for disruptive agents as previously reported[12]. Guided by the structural features of the U-shaped TM5/6 loop in HACD, we synthesized three peptides of varying lengths, designated L1-L3 (Fig. 7c). The L3 peptide covers the entire U-shaped loop region (residues 201-212) of HsHACD2, including key residues for both conformational stability and TECR

interaction (Fig. 7c). In contrast, the shorter L1 (residues 203-210) and L2 (residues 202-211) peptides retain critical interfacial residues but lack the intra-peptide interactions mediated by I202 and F212 (Fig. 7c). In a peptide competition assay, the immobilized HACD2-TECR complex was incubated with each peptide for competitive binding (Fig. 7b), followed by elution and western blot analysis. The results showed that L1 and L2 peptides disrupted 25% and 40% of the HACD-TECR complex, respectively, while the longer L3 peptide disrupted 50%, exhibiting higher potency (Fig. 7d). In contrast, the mutated peptides (M1-M4), which compromise key interactions, failed to compete with HACD2 for binding to TECR (Fig. 7c and d). The competition assay offers a robust platform for screening potent modulators to disrupt the HACD-TECR interface, potentially serving as lead compounds to impair CRC growth.

Colorectal cancer (CRC) is the third most common cancer and the second leading cause of cancer-related deaths globally[38]. Standard treatments include surgery, chemotherapy, targeted therapy, and immunotherapy, with available options such as VEGFR inhibitors, BRAF inhibitors, anti-EGFR monoclonal antibodies, and immune checkpoint inhibitors[28]. However, limited effectiveness of targeted therapy and low response rate of immunotherapy in certain CRC subtypes emphasize the need for more effective and tailored therapeutic strategies. Previous studies on lipid metabolism in CRC have primarily focused on fatty acid oxidation for energy production and the immunosuppressive effects of altered lipids, with the role of VLCFAs remaining unclear[39-41]. Hijacking VLCFA metabolism may serve as an alternative therapeutic strategy for CRC, warranting further research into its impact on tumor growth regulation. Beyond the HACD-TECR subcomplex, other subcomplexes like ELOVL-KAR also play roles in VLCFA elongation. Understanding the mechanisms of the entire VLCFA elongation process is crucial for targeted modulation of VLCFA biosynthesis in cancer treatment.

Methods

Protein expression and purification

The cDNA sequences of human ELOVL3, KAR, HACD2, and TECR were codon-optimized and individually cloned into the pMLink vector with C-terminal tags as follows: ELOVL3-Flag, KAR-Flag, HACD2-His, and TECR-Flag. All mutants were produced using a standard PCR-based approach. Expi293F cells cultured in FreeStyle 293 medium (Union Biotech; UP1000) at a density of 1.5~2.0 × 10^6 cells/mL were transiently transfected with PEI 4000 at a plasmid to PEI ratio of 1:3 (w/w). For each liter of culture, a total of 1 mg of plasmid was used. For the coexpression of HACD2-TECR complex, the HACD2 and TECR plasmids were co-transfected with a 1:1 ratio (w/w). The cells were cultured for 48 hours and harvested by centrifugation.

For protein purification, the cell lysis was mechanically homogenized in dounce and clarified by ultracentrifugation (55,000 × g, 1 hour, 4 °C). The collected membrane was extracted by 1% w/v lauryl maltose neopentyl glycol (LMNG; Anatrace) and 0.1% w/v cholesteryl hemisuccinate (CHS; Anatrace) in the presence of protease inhibitors at 4 °C for 2 hours. Insoluble debris was removed by ultracentrifugation (55,000 × g, 1 hour, 4 °C), and the supernatant was collected for affinity purification. For the HACD2-TECR complex purification, the supernatant was incubated with the anti-Flag G1 affinity resin (GenScript; L00432-1) at 4 °C for 1 hour. The resin was washed with buffer A (25 mM HEPES pH 7.5, 150 mM NaCl, 5% glycerol) containing 0.02% (w/v) glyco-diosgenin (GDN; Anatrace) and eluted in the same buffer supplemented with 200 μg/mL Flag peptide (Every lab; PF03-20). The eluate was further purified by nickel-affinity chromatography. Upon binding with Ni-NTA affinity resin (Qiagen; 17371201), the resin was washed with buffer A plus 0.02% GDN and 25 mM imidazole, then eluted

using buffer A with 0.01% GDN and 250 mM imidazole. The elution was concentrated and subjected to size-exclusion chromatography (SEC) on a Superose 6 Increase 10/300 GL column (GE Healthcare) equilibrated in buffer A containing 0.005% GDN. Protein fractions were collected for crosslinking and structural studies. The proteins used for the in vitro reconstitution of VLCFA elongation assay was prepared similarly. The ELOVL3 and KAR proteins were purified by anti-Flag affinity chromatography, and the HACD2-TECR complex was purified by nickel-affinity chromatography. After affinity purification, the proteins were further purified by SEC on a Superdex 200 Increase column (Cytiva) equilibrated in buffer B (25 mM HEPES pH 7.5, 150 mM NaCl, 2% glycerol, 0.01% LMNG, 0.001% CHS).

The *C. elegans* HACD-TECR complex was expressed in insect cells and purified similarly. Briefly, the cDNA sequences of *C. elegans* HACD and TECR were codon-optimized and subcloned into pFastBac vector with N-terminal His tag and no tag, respectively. Baculovirus was produced via the Bac-to-Bac system (Invitrogen) and employed to infect Sf9 cells. The HACD-TECR complex was extracted by 1% LMNG plus 0.1% CHS in the presence of protease inhibitors, purified through nickel-affinity chromatography, and eluted in buffer B plus 250 mM imidazole. The concentrated elute was incubated with 200 μM NADPH at 4 °C for 1 hour before being applied to SEC on a Superdex 200 Increase column (Cytiva) equilibrated in buffer B. The peak fractions were collected for structural studies.

In vitro VLCFA elongation assay

A typical VLCFA elongation reaction mixture contained 10 μM 18:0-CoA, 50 μM ^{13}C-labeled malonyl-CoA, 1 mM NADPH, 2 mM $MgCl_2$, 1 mM $CaCl_2$, and 0.01 mg/mL fatty acid-free BSA in buffer B. A total of 10 μg human VLCFA elongation enzymes (6 μg ELOVL3, 3 μg KAR, 1 μg HACD2-TECR complex) were added into 50 μL of reaction mixture to initialize the reaction. Reactions were incubated at 20 °C

for 2 hours. The lipids were saponified to release free fatty acids using an alkaline hydrolysis–liquid–liquid extraction procedure. Briefly, the reaction mixture sample was hydrolyzed by the addition of methanolic potassium hydroxide (1 mol/L), followed by incubation at 60 °C with agitation for 1 h. After hydrolysis, the samples were cooled to room temperature and subsequently acidified with citric acid to pH < 2 to minimize undesired isomerization of unsaturated fatty acids. Fatty acids were recovered by three consecutive liquid–liquid extractions using n-hexane containing 0.01% (w/w) butylated hydroxytoluene (BHT) as an antioxidant. After centrifugation, the organic phases were collected, combined, and evaporated to dryness under a gentle nitrogen stream. The residue was reconstituted in methanol/isopropanol (1:1, v/v) prior to LC–HRMS analysis.

LC–HRMS analysis

Liquid chromatography–high-resolution mass spectrometry (LC–HRMS) analysis was performed using a high-resolution quadrupole Orbitrap mass spectrometer (Q Exactive™, Thermo Fisher Scientific, USA) equipped with an electrospray ionization (ESI) source and coupled to an ACQUITY UPLC I-Class system (Waters, USA). Chromatographic separation was achieved on a Waters ACQUITY CSH C18 column (2.1 × 100 mm, 1.7 μm), with the column temperature maintained at 55 °C. The mobile phases consisted of solvent A (10 mM ammonium acetate with 0.1% formic acid in acetonitrile/water, 60:40, v/v) and solvent B (10 mM ammonium acetate with 0.1% formic acid in isopropanol/acetonitrile, 90:10, v/v). Gradient elution was applied as follows: 60% A at 0 min, decreased to 57% A at 3 min, 50% A at 3.1 min, 46% A at 13 min, and 30% A at 13.1 min, followed by a decrease to 1% A at 20 min. The column was then re-equilibrated at 60% A until 25 min. The flow rate was 0.36 mL/min. MS data were acquired in negative ion mode. The sheath gas pressure was set to 40 arb, auxiliary gas pressure to 10 arb, and sweep gas pressure to 1 arb. The spray voltage was set to −3.2 kV. The capillary temperature was

maintained at 320 °C, and the auxiliary gas heater temperature was set to 450 °C. Full-scan MS spectra were acquired over an m/z range of 200–500 with a resolving power of 140,000 (FWHM).

Raw LC–HRMS data were processed using Compound Discoverer software (v3.3, Thermo Fisher Scientific, USA) with the Stable Isotope Labeling workflow. The workflow performs feature detection and alignment across samples, followed by extraction of isotope-resolved ion chromatograms for labeled and unlabeled isotopologues. Natural isotope abundance correction was applied to remove the contribution of naturally occurring isotopes to the measured isotopic patterns. For each fatty acid, isotopologue distributions (M, M+1, M+2, etc.) were obtained based on accurate mass and chromatographic retention time. The corrected mass isotopic distributions were used to calculate isotope enrichment and labeling patterns.

Cryo-EM sample preparation and data acquisition

For sample preparation, 3.5 μL of human HACD2-TECR complex at a concentration of 15-24 mg/ml or *C. elegans* HACD-TECR complex at a concentration of 10-15 mg/ml was applied to glow-discharged holey carbon-coated grids (Quantifoil 300 mesh, Au R1.2/1.3) or holey nickel-titanium coated gold grids (CryoMatrix M024-Au300-R12/13). The grids were blotted for 3s and flash-frozen in liquid ethane using a Vitrobot (Mark IV, Thermo Fisher Scientific). Images were recorded on a 300kV Titan Krios G3i electron microscope (Thermo Fisher Scientific) equipped with Gatan K3 Summit direct detector and a GIF Quantum energy filter (slit width 20 eV). Movie stacks of human HACD2-TECR complex were collected using SerialEM[42] in counting mode at a magnification of 105,000x with the corresponding pixel size of 0.83 Å. Each movie stack consisted of 50 frames and was exposed for 2.5 s or 3 s. Several batches of movie stacks at a dose rate of 12.33-15.95 e^-/px/s were recorded, resulting in a total dose of about

50.67-58.09 $e^-/Å^2$. The defocus range was set from −1.0 μm to −2.0 μm. A total of 16,425 and 14,810 movie stacks were collected for the non-crosslinked and crosslinked HACD2-TECR complexes, respectively. Movie stacks of *C. elegans* HACD-TECR complex were recorded similarly in super-resolution mode at a magnification of 105,000x with the corresponding pixel size of 0.425 Å. Movie stacks with 50 frames were exposed for 2s. Several batches of movie stacks at a dose rate of 18.28-19.06 e^-/px/s were collected, corresponding to a total dose of about 50.6-52.76 $e^-/Å^2$. The defocus range was set from −1.5 μm to −2.0 μm. A total of 19,116 movie stacks were collected.

Cryo-EM data processing

Movie frames were aligned using MotionCor2[43]. Micrograph contrast transfer function (CTF) estimations were performed using micrographs without dose-weighting. Particles were automatically picked by Gautomatch (https://www.mrc-lmb.cam.ac.uk/kzhang/Gautomatch).

For the non-crosslinked human HACD2-TECR complex, 14,367 micrographs with estimated Ctf Max Resolution (> 5 Å) and Ctf Figure of Merit (> 0.2) were selected for further processing. A total of 4,845,240 particles were extracted for iterative 2D classifications using cryoSPARC v.2.14.2[44]. Subsequently, 1,227,014 particles were selected for multiple rounds of ab initio reconstruction and heterogeneous refinement. For the crosslinked human HACD2-TECR complex, 13,634 micrographs with estimated Ctf Max Resolution (> 4 Å) and Ctf Figure of Merit (> 0.25) were selected for further processing. In total, 4,851,341 particles were extracted for multiple rounds of 2D classification and ab initio reconstruction, yielding a subset of 67,876 particles. The particles were used for a further round of ab initio reconstruction and non-uniform refinement, yielding a final reconstruction map at 6.32 Å resolution.

For the *C. elegans* HACD-TECR complex, 35,015,130 particles from 19,116 micrographs were picked. After multiple rounds of 2D classification and ab initio reconstruction, 291,236 good quality particles were selected. A subsequent round of ab initio reconstruction followed by non-uniform refinement generated a 3D density map at a resolution of 4.27 Å. Further 2D classification, ab initio reconstruction, heterogeneous refinement, and non-uniform refinement improved the map resolution to 3.94 Å. Subsequent particle curation was performed using the CryoSieve script, which selected 131,428 high-quality particles. These were refined through one round of ab initio reconstruction, non-uniform refinement, and local refinement, ultimately producing a final 3D density map at a resolution of 3.6 Å.

Model building and refinement

Initial structural models for TECR and HACD were generated using AlphaFold2 predictions. These models were fitted into the EM density map using chimera, and followed by iterative rounds of manual building in Coot[45]. The final model was subjected to a real space refinement in Phenix[46]. All structural figures were prepared in PyMOL or UCSF Chimera[47] and UCSF ChimeraX[48].

Statistical analyses

The statistical analysis of all data in this study was conducted using GraphPad Prism 9.0 software. The data are presented as mean ± SD or median with range. One-way ANOVA, two-way ANOVA, two-tailed Student's t test, Wilcoxon signed-rank test and the Mann-Whitney U test were performed to compare the differences between groups. Significance levels were defined as follows: *P < 0.05, **P < 0.01, ***P < 0.001, ****P < 0.0001, and ns indicates no significant difference.

Data availability

The EM density map and atomic coordinates for the *C. elegans* HACD-TECR complex have been deposited in the EMDB under accession code EMD-68536 and in the PDB under the accession code 22OF, respectively. The EM density map for the human HACD2-TECR complex has been deposited in the EMDB under accession code EMD-38493.

Acknowledgments

We gratefully acknowledge the Cryo-EM Facility at the School of Life Sciences, Fudan University, for their support; the Cryo-EM Center of the Kobilka Institute at the Chinese University of Hong Kong, Shenzhen, for cryo-EM image acquisition; and the core facility of the Institute of Metabolism & Integrative Biology at Fudan University for LC-MS data collection. R.R was supported by Shanghai Eastern Talent Plan Youth Project and Fudan University Outstanding Youth Talent Plan. This work was supported by the National Natural Science Foundation of China (grant no 82273025 to Yunshi Zhong; grant no 32422048 to Li Chen), National Key R&D Program “Strategic Scientific and Technological Innovation Cooperation” Key Project (2022YFE0203600 to Jia Liu), Shanghai Municipal Health Commission Projects (202340178 and 202540081), Shanghai Hospital Deveopment Center SHDC12026125, Shanghai Innovative Medical Devices and Pharmaceuticals Application Demonstration Project (25SF1906800), and Clinical Research Special Project of Zhongshan Hospital, Fudan University (ZSLCYJ202350).

Author Contributions

R.R conceived the project and designed all experiments. R.L. and Y.Z. conducted all clones, purified protein samples for EM data collection of *C.elegans* and human respectively. R.L. reconstituted the in

vitro systems. L.Y. and H.J. prepared the Cryo-EM grids and collected the EM data. L.Y. determined structures. J.L. performed the in vivo experiments and carried out the bioinformatics analysis. R.T. performed docking, MD simulations based on structural and biochemical results. R.H. helped to collect samples, operated LC-MS equipment and analyzed the data. C.W. developed and implemented the experimental methods. B.S., Y.C. and F.L. conducted the experimental investigations. M.G., H.H., S.Y., P.Z., L.Z., and M.C. validated the data processing. J.L. and L.C. supervised the LC-MS data analysis. Y.Z. provided essential research resources. R.R. and T.X. wrote the manuscript. All authors analyzed the data and contributed to manuscript preparation.

Competing interests: The authors declare no competing interests.

References

1. Jakobsson, A., R. Westerberg, and A. Jacobsson, *Fatty acid elongases in mammals: their regulation and roles in metabolism.* Prog Lipid Res, 2006. **45**(3): p. 237-49.
2. Kyselová, L., M. Vítová, and T. Řezanka, *Very long chain fatty acids.* Prog Lipid Res, 2022. **87**: p. 101180.
3. Yeboah, G.K., et al., *Very long chain fatty acid-containing lipids: a decade of novel insights from the study of ELOVL4.* J Lipid Res, 2021. **62**: p. 100030.
4. Kihara, A., *Very long-chain fatty acids: elongation, physiology and related disorders.* J Biochem, 2012. **152**(5): p. 387-95.
5. Sassa, T. and A. Kihara, *Metabolism of very long-chain Fatty acids: genes and pathophysiology.* Biomol Ther (Seoul), 2014. **22**(2): p. 83-92.
6. Wang, X., et al., *A comprehensive review of the family of very-long-chain fatty acid elongases: structure, function, and implications in physiology and pathology.* Eur J Med Res, 2023. **28**(1): p. 532.
7. Guillou, H., et al., *The key roles of elongases and desaturases in mammalian fatty acid metabolism: Insights from transgenic mice.* Prog Lipid Res, 2010. **49**(2): p. 186-99.
8. Moon, Y.A. and J.D. Horton, *Identification of two mammalian reductases involved in the two-carbon fatty acyl elongation cascade.* J Biol Chem, 2003. **278**(9): p. 7335-43.
9. Ikeda, M., et al., *Characterization of four mammalian 3-hydroxyacyl-CoA dehydratases involved in very long-chain fatty acid synthesis.* FEBS Lett, 2008. **582**(16): p. 2435-40.
10. Ohno, Y., et al., *ELOVL1 production of C24 acyl-CoAs is linked to C24 sphingolipid synthesis.* Proc Natl Acad Sci U S A, 2010. **107**(43): p. 18439-44.
11. Kato, R., et al., *Catalytic mechanism of trans-2-enoyl-CoA reductases in the fatty acid elongation cycle and its cooperative action with fatty acid elongases.* J Biol Chem, 2024. **300**(2): p. 105656.
12. Zhou, Y., et al., *The 3-hydroxyacyl-CoA dehydratase 1/2 form complex with trans-2-enoyl-CoA reductase involved in substrates transfer in very long chain fatty acid elongation.* Biochem Biophys Res Commun, 2024. **704**: p. 149588.
13. Denic, V. and J.S. Weissman, *A molecular caliper mechanism for determining very long-chain fatty acid length.* Cell, 2007. **130**(4): p. 663-77.
14. Konishi, H., et al., *Characterization of HACD1 K64Q mutant found in arrhythmogenic right ventricular dysplasia patients.* J Biochem, 2010. **148**(5): p. 617-22.
15. Okuda, A., et al., *Hetero-oligomeric interactions of an ELOVL4 mutant protein: implications in the molecular mechanism of Stargardt-3 macular dystrophy.* Mol Vis, 2010. **16**: p. 2438-45.
16. Naganuma, T. and A. Kihara, *Two modes of regulation of the fatty acid elongase ELOVL6 by the 3-ketoacyl-CoA reductase KAR in the fatty acid elongation cycle.* PLoS One, 2014. **9**(7): p. e101823.
17. Abe, K., et al., *Mutation for nonsyndromic mental retardation in the trans-2-enoyl-CoA reductase TER gene involved in fatty acid elongation impairs the enzyme activity and stability, leading to change in sphingolipid profile.* J Biol Chem, 2013. **288**(51): p. 36741-9.
18. Hoy, A.J., S.R. Nagarajan, and L.M. Butler, *Tumour fatty acid metabolism in the context of*

therapy resistance and obesity. Nat Rev Cancer, 2021. **21**(12): p. 753-766.
19. Snaebjornsson, M.T., S. Janaki-Raman, and A. Schulze, *Greasing the Wheels of the Cancer Machine: The Role of Lipid Metabolism in Cancer.* Cell Metab, 2020. **31**(1): p. 62-76.
20. Jin, H.R., et al., *Lipid metabolic reprogramming in tumor microenvironment: from mechanisms to therapeutics.* J Hematol Oncol, 2023. **16**(1): p. 103.
21. Tamura, K., et al., *Novel lipogenic enzyme ELOVL7 is involved in prostate cancer growth through saturated long-chain fatty acid metabolism.* Cancer Res, 2009. **69**(20): p. 8133-40.
22. Wan, M., et al., *Lipid metabolic reprograming: the unsung hero in breast cancer progression and tumor microenvironment.* Mol Cancer, 2025. **24**(1): p. 61.
23. Röhrig, F. and A. Schulze, *The multifaceted roles of fatty acid synthesis in cancer.* Nat Rev Cancer, 2016. **16**(11): p. 732-749.
24. Hama, K., et al., *Very long-chain fatty acids are accumulated in triacylglycerol and nonesterified forms in colorectal cancer tissues.* Sci Rep, 2021. **11**(1): p. 6163.
25. Marien, E., et al., *Phospholipid profiling identifies acyl chain elongation as a ubiquitous trait and potential target for the treatment of lung squamous cell carcinoma.* Oncotarget, 2016. **7**(11): p. 12582-97.
26. Yamashita, Y., et al., *Differences in elongation of very long chain fatty acids and fatty acid metabolism between triple-negative and hormone receptor-positive breast cancer.* BMC Cancer, 2017. **17**(1): p. 589.
27. Chu, Q., et al., *Stearate-derived very long-chain fatty acids are indispensable to tumor growth.* Embo j, 2023. **42**(2): p. e111268.
28. Xie, Y.H., Y.X. Chen, and J.Y. Fang, *Comprehensive review of targeted therapy for colorectal cancer.* Signal Transduct Target Ther, 2020. **5**(1): p. 22.
29. Liu, Y., et al., *Genome-wide circular RNA (circRNA) and mRNA profiling identify a circMET-miR-410-3p regulatory motif for cell growth in colorectal cancer.* Genomics, 2022. **114**(1): p. 351-360.
30. Lee, H.O., et al., *Lineage-dependent gene expression programs influence the immune landscape of colorectal cancer.* Nat Genet, 2020. **52**(6): p. 594-603.
31. Han, Y., et al., *Crystal structure of steroid reductase SRD5A reveals conserved steroid reduction mechanism.* Nat Commun, 2021. **12**(1): p. 449.
32. Xiao, Q., et al., *Structure of human steroid 5alpha-reductase 2 with the anti-androgen drug finasteride.* Nat Commun, 2020. **11**(1): p. 5430.
33. Nie, L., et al., *The structural basis of fatty acid elongation by the ELOVL elongases.* Nat Struct Mol Biol, 2021. **28**(6): p. 512-520.
34. Kihara, A., et al., *Membrane topology and essential amino acid residues of Phs1, a 3-hydroxyacyl-CoA dehydratase involved in very long-chain fatty acid elongation.* J Biol Chem, 2008. **283**(17): p. 11199-209.
35. Aggarwal, S., et al., *An overview on 5alpha-reductase inhibitors.* Steroids, 2010. **75**(2): p. 109-53.
36. Cilotti, A., G. Danza, and M. Serio, *Clinical application of 5alpha-reductase inhibitors.* J Endocrinol Invest, 2001. **24**(3): p. 199-203.
37. Roehrborn, C.G., et al., *Efficacy and safety of a dual inhibitor of 5-alpha-reductase types*

1 and 2 (dutasteride) in men with benign prostatic hyperplasia. Urology, 2002. **60**(3): p. 434-41.

38. Bray, F., et al., *Global cancer statistics 2018: GLOBOCAN estimates of incidence and mortality worldwide for 36 cancers in 185 countries.* CA Cancer J Clin, 2018. **68**(6): p. 394-424.
39. Huang, T.X., et al., *ATP6V0A1-dependent cholesterol absorption in colorectal cancer cells triggers immunosuppressive signaling to inactivate memory CD8(+) T cells.* Nat Commun, 2024. **15**(1): p. 5680.
40. Mana, M.D., et al., *High-fat diet-activated fatty acid oxidation mediates intestinal stemness and tumorigenicity.* Cell Rep, 2021. **35**(10): p. 109212.
41. Liu, X., et al., *Reprogramming lipid metabolism prevents effector T cell senescence and enhances tumor immunotherapy.* Sci Transl Med, 2021. **13**(587).
42. Mastronarde, D.N., *SerialEM: A Program for Automated Tilt Series Acquisition on Tecnai Microscopes Using Prediction of Specimen Position.* Microscopy and Microanalysis, 2003. **9**(S02): p. 1182-1183.
43. Zheng, S.Q., et al., *MotionCor2: anisotropic correction of beam-induced motion for improved cryo-electron microscopy.* Nat Methods, 2017. **14**(4): p. 331-332.
44. Punjani, A., et al., *cryoSPARC: algorithms for rapid unsupervised cryo-EM structure determination.* Nat Methods, 2017. **14**(3): p. 290-296.
45. Emsley, P. and K. Cowtan, *Coot: model-building tools for molecular graphics.* Acta Crystallogr D Biol Crystallogr, 2004. **60**(Pt 12 Pt 1): p. 2126-32.
46. Adams, P.D., et al., *PHENIX: a comprehensive Python-based system for macromolecular structure solution.* Acta Crystallogr D Biol Crystallogr, 2010. **66**(Pt 2): p. 213-21.
47. Pettersen, E.F., et al., *UCSF Chimera--a visualization system for exploratory research and analysis.* J Comput Chem, 2004. **25**(13): p. 1605-12.
48. Pettersen, E.F., et al., *UCSF ChimeraX: Structure visualization for researchers, educators, and developers.* Protein Sci, 2021. **30**(1): p. 70-82.

636 **Main Figures**

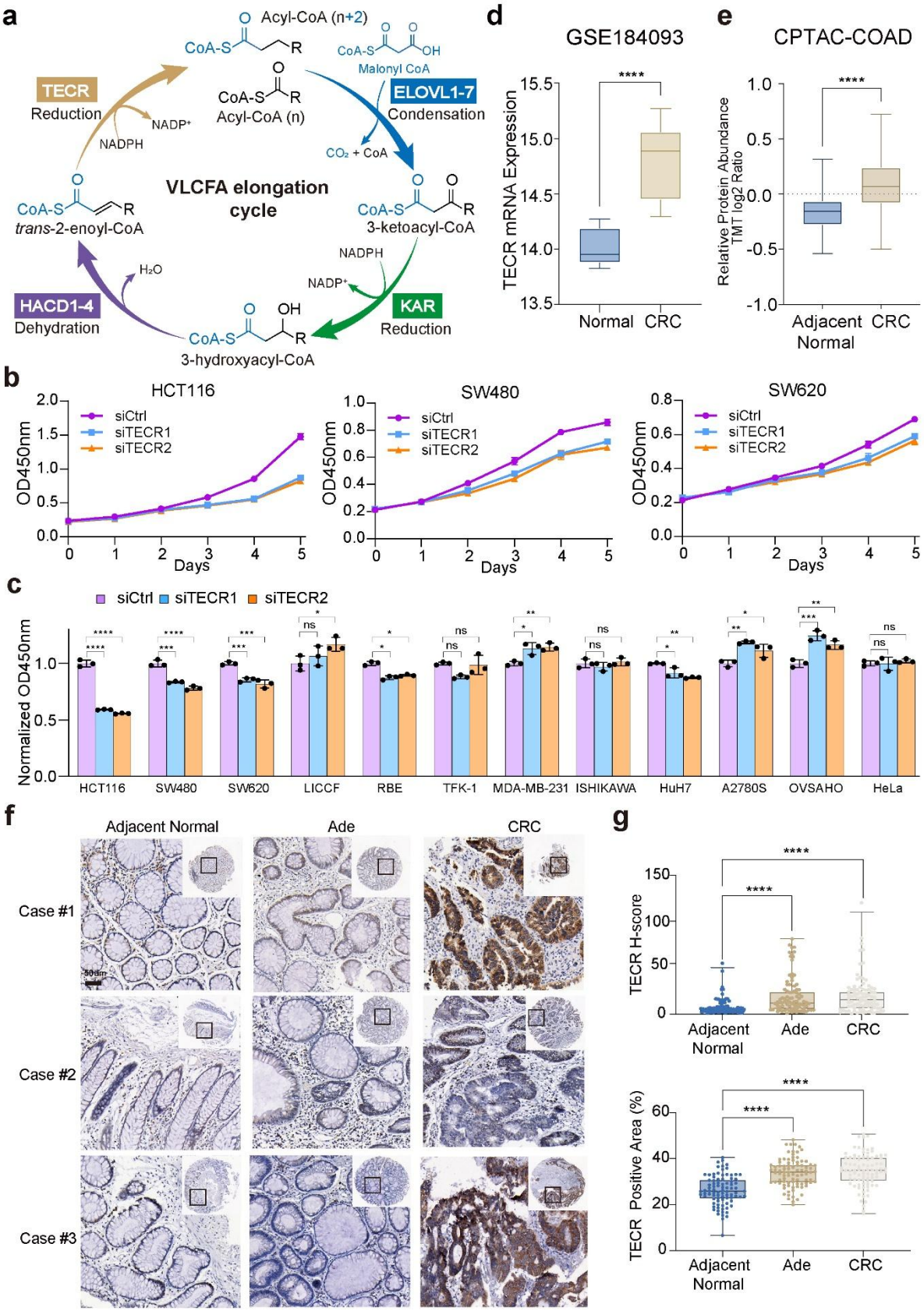

637

638 **Fig. 1** | **TECR is associated with CRC cell proliferation and tumorigenesis. a,** Schematic
639 illustration of the VLCFA elongation cycle catalyzed by ELOVL, KAR, HACD, and TECR. **b,** TECR
640 knockdown specifically suppress CRC cell proliferation. **c,** Statistic analysis of cell proliferation of
641 various cancer cell lines upon TECR knockdown. **d,** Comparison of transcriptome of TECR between
642 normal and CRC tissues analyzed from the Gene Expression Omnibus (GEO) dataset GSE184093. **e,**
643 Comparison of the TECR protein expression levels between CRC and the adjacent normal tissues
644 analyzed from the Clinical Proteomic Tumor Analysis Consortium (CPTAC) dataset for the colon
645 adenocarcinoma (COAD). **f,** Representative images of the immunohistochemistry (IHC) analysis of the
646 carcinoma, adenoma, and adjacent normal tissues from three cases. **g,** Quantitative IHC analysis of
647 the carcinoma, adenoma, and adjacent normal tissues from 87 cases. Data are representative of three
648 independent experiments (b, c). Error bars are mean ± SD. *P < 0.05, **P < 0.01, ***P < 0.001, ****P <
649 0.0001 by one-way ANOVA multiple comparisons test (c), and Student's t test (d-e, g); ns, not
650 significant. Box plots indicate the median (center line) and range (whiskers: min to max).
651
652
653

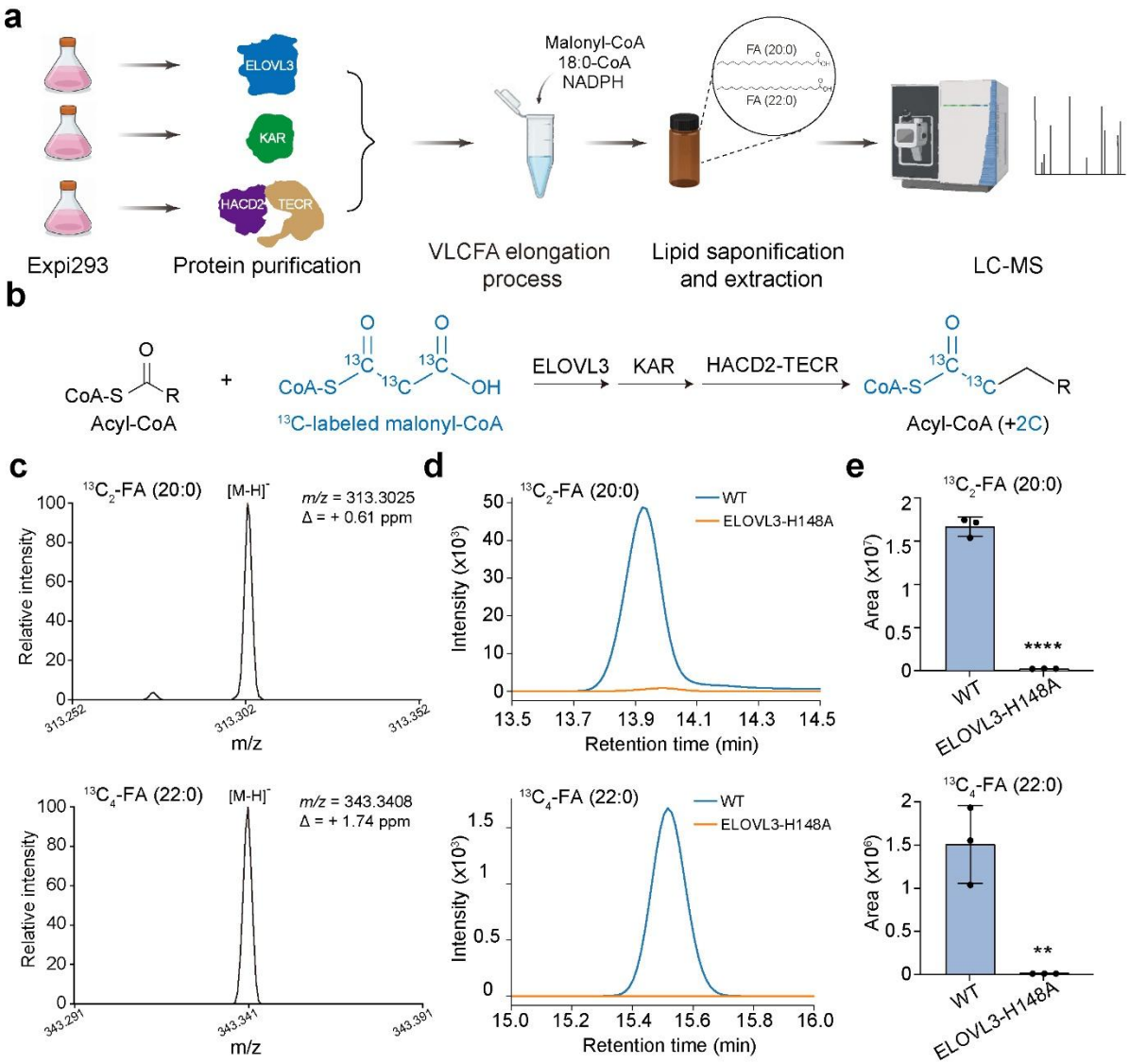

Fig. 2 | **In vitro reconstitution of the VLCFA elongation assay. a,** Flowchart outlining the in vitro VLCFA elongation assay system. **b,** Schematic diagram of the VLCFA elongation assay using ^{13}C-labeled malonyl-CoA substrate. **c,** MS analysis of ^{13}C-labeled fatty acid (20:0) and fatty acid (22:0) saponified from the acyl-CoA elongation products generated by the VLCFA elongation complex. **d,** Comparison of extracted ion chromatograms (EICs) for fatty acid (20:0) and fatty acid (22:0) saponified from acyl-CoA elongation products generated by WT elongation complex and catalytic inactive elongation complex containing ELOVL3-H148A mutant. **e**, Quantification of fatty acid (20:0) and fatty acid (22:0) saponified from acyl-CoA elongation products generated by WT and ELOVL3-

H148A mutant. Data are representative of three independent experiments. Error bars are mean ± SD.

**P < 0.01, ****P < 0.0001 by Student's t test.

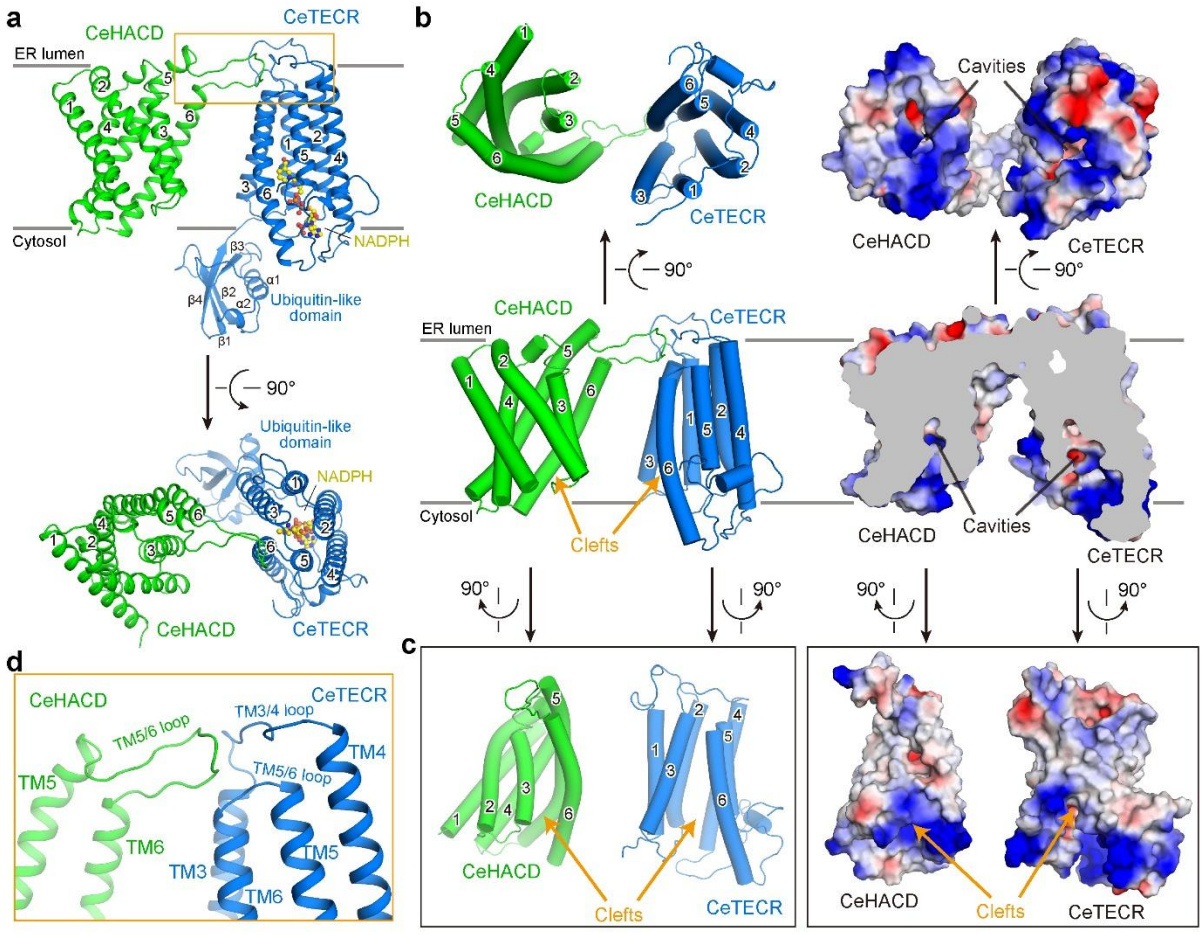

Fig. 3 | **Structural determination of the *C. elegans* HACD-TECR complex. a,** Perpendicular views of the HACD-TECR complex. HACD and TECR are colored green and blue, respectively. The NADPH cofactor is shown in yellow spheres. **b,** Perpendicular views of the central cavities within HACD and TECR transmembrane domains facing the cytosolic side of membrane. Electrostatic surface potentials of the HACD-TECR complex are colored blue and red for positive and negative charges, respectively. **c,** Opposing lateral clefts formed by HACD-TM3/6 and TECR-TM3/6. **d,** The HACD TM5/6 luminal loop is in close proximity to the TM3/4 and TM5/6 luminal loops of TECR.

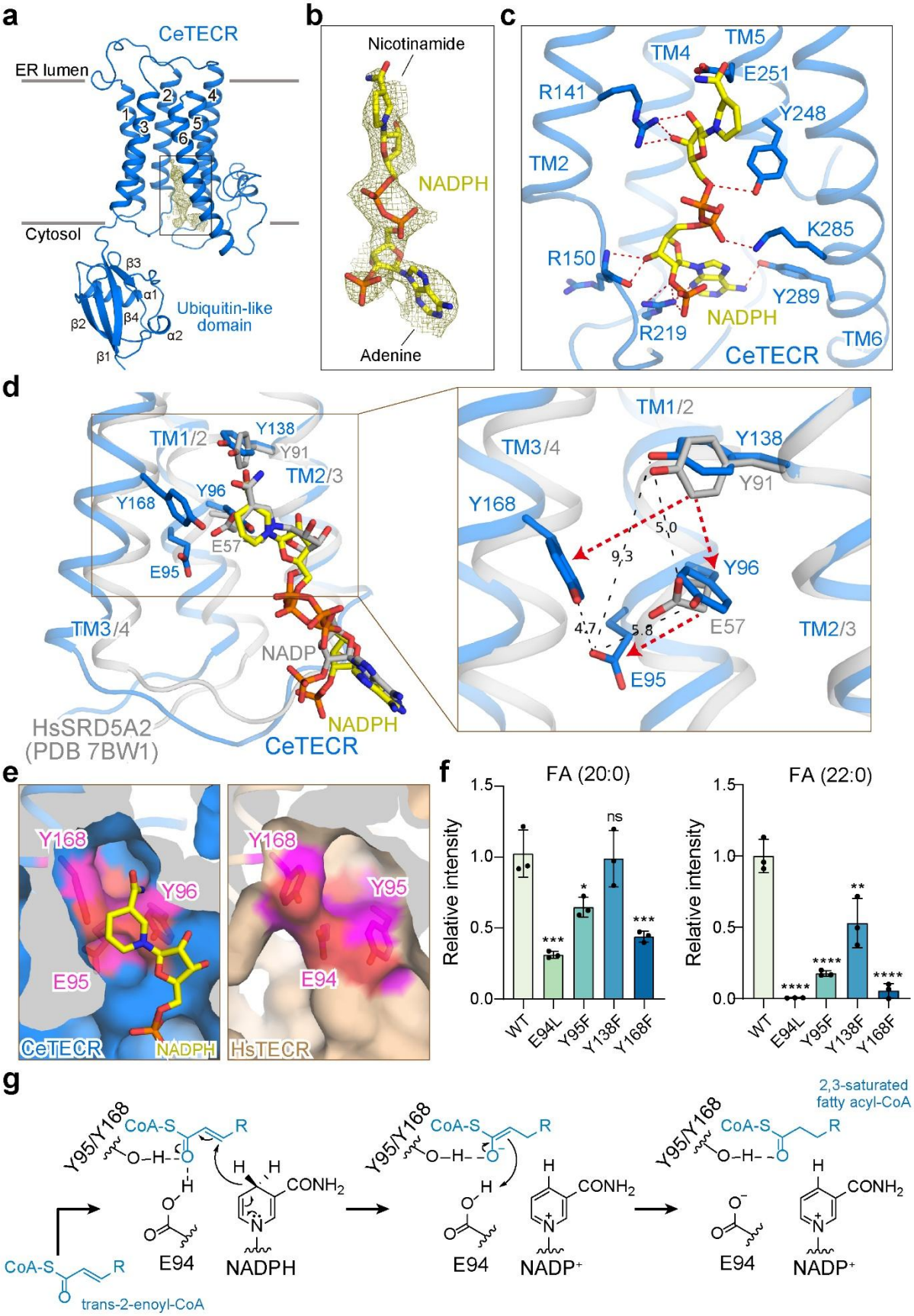

679

680 **Fig. 4 | Catalytic mechanism of TECR. a,** Overall structure the *C. elegans* TECR subunit. **b,** EM

density of the NADPH cofactor contoured at 5σ. **c,** Close-up view of the NADPH coordinating interface on TECR. The hydrogen-bonds between NADPH and TECR are shown by red dashed lines. **d,** Superimposition of the catalytic residues of TECR and SRD5A2 reductases. The NADP-dihydrofinasteride bound SRD5A2 (PDB 7BW1) is colored light grey. The NADPH-bound TECR is colored blue. The catalytic residues on TECR and SRD5A2 are shown in sticks. **e,** Potential catalytic tyrosine residues located near the catalytic glutamate residue on TECR catalytic pocket. The catalytic pockets on *C. elegans* TECR and human TECR are shown in blue and wheat, respectively. The potential catalytic tyrosine residues and catalytic glutamate residue on each pocket are highlighted in magenta. **f,** Functional characterization of the catalytic residues on TECR by the in vitro VLCFA elongation assay. The activities of TECR mutants were normalized relative to that of the WT. Data are representative of three independent experiments. Error bars are mean ± SD. *P < 0.05, **P < 0.01, ***P < 0.001, ****P < 0.0001 by one-way ANOVA multiple comparisons test; ns, not significant; asterisk shows comparison with wild-type. **g,** Proposed reduction mechanism of human TECR. The glutamate residue likely collaborates with either tyrosine residues to coordinate the trans-2-enoyl-CoA substrate to facilitate hydride ion transfer from NADPH.

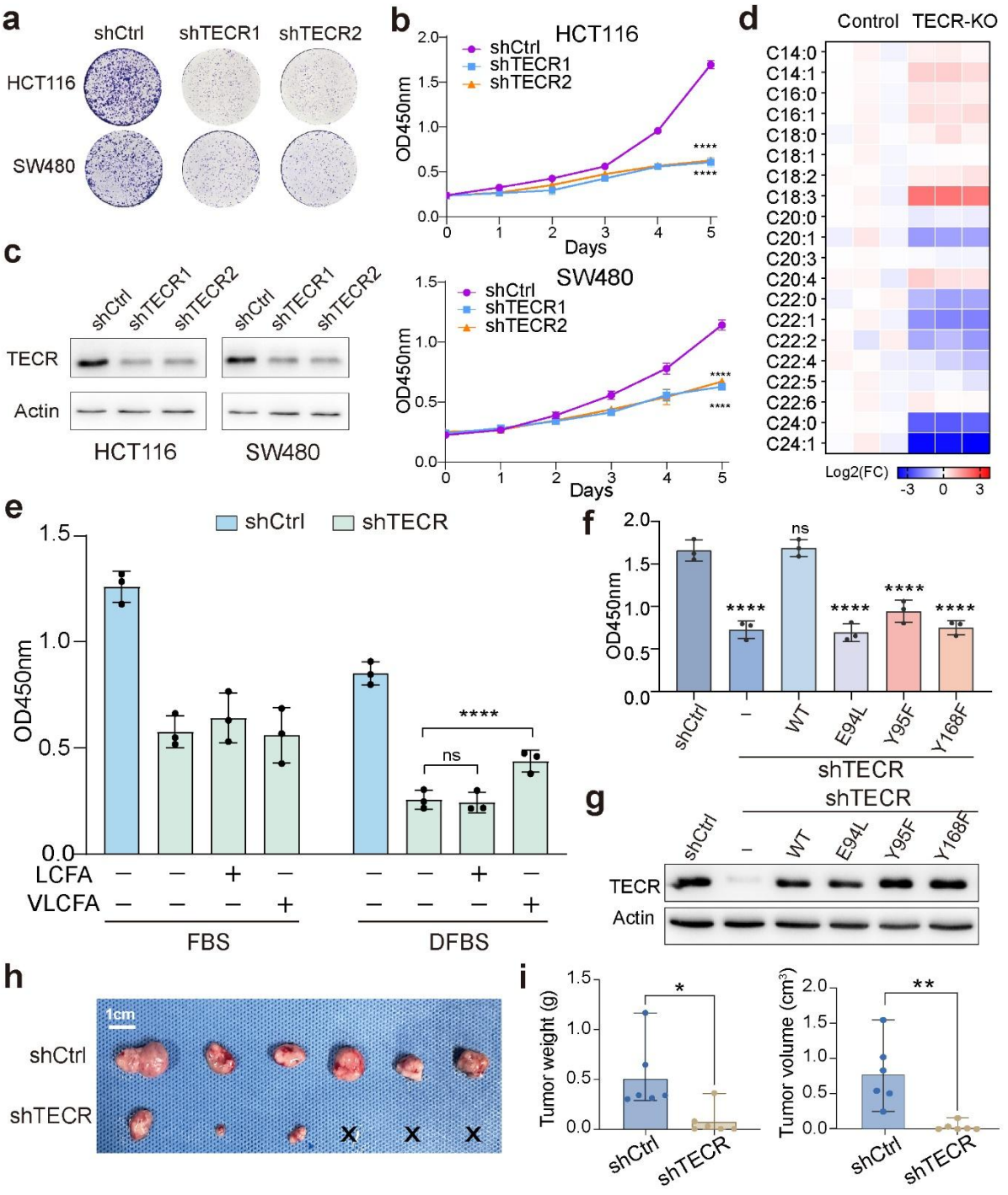

Fig. 5 | TECR knockdown impair VLCFA synthesis in CRC cells and suppresses tumorigenesis.

a, Colony formation analysis of HCT116 and SW480 cells stably transduced with control shRNA or TECR shRNAs (shTECR1 or shTECR2). **b,** Cell viability of HCT116 and SW480 cells stably transduced with control shRNA or TECR shRNAs (shTECR1 or shTECR2) determined by CCK-8 assay. **c,** TECR expression levels in control and stable TECR knockdown cells determined by western

blotting (WB). Actin was the endogenous control. **d,** Heatmap of differential profiles of fatty acids of HCT116 cells transduced with control or TECR sgRNAs. **e,** Proliferation rate of TECR knockdown HCT116 cells in FBS medium or delipidized FBS (DFBS) medium supplemented without or with LCFAs (2 μM FA 16:0, 2 μM FA 18:0) or VLCFAs (2 μM FA 22:0, 2 μM FA 24:0, 2 μM FA 26:0). **f,** Impaired TECR activity suppress HCT116 cell proliferation. **g,** Western blot analysis of TECR expression. **h,** Image of xenograft tumors excised from BALB/c nude mice subcutaneously injected with control or TECR knockdown HCT116 cells (n = 6). **i,** Statistics of tumor weight and tumor volume of the mice shown in **h**. Data are representative of three (b, e, f) or six (h, i) independent experiments. Error bars represent mean ± SD. ****P < 0.0001 by one-way ANOVA multiple comparisons test (b, e, f); ns, not significant; asterisk shows comparison between shTECR groups and control group (b, f). Data are median with range and the P value of two-tailed Mann Whitney test, *P < 0.05, **P < 0.01 (i).

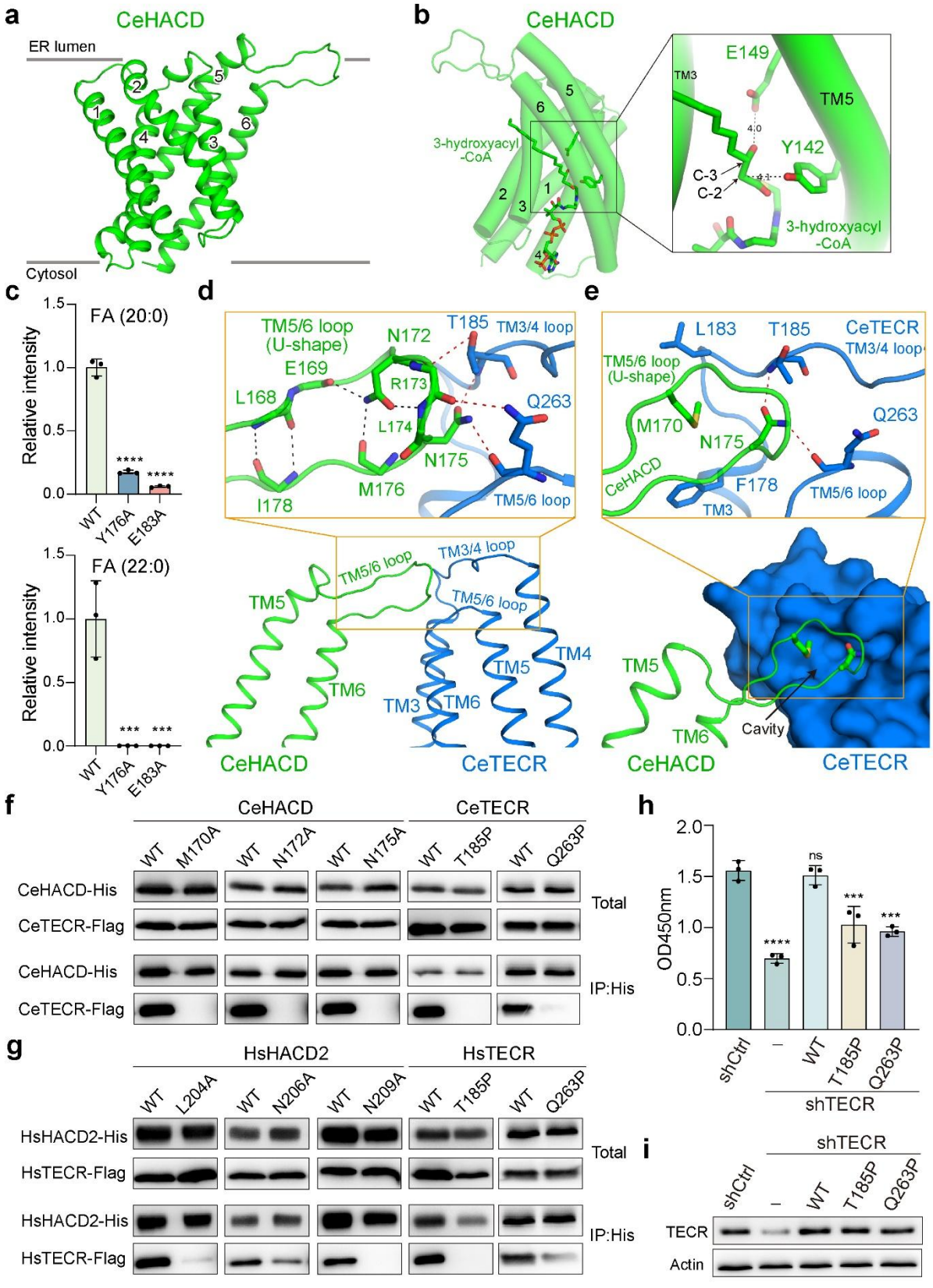

Fig. 6 | **Disruption of the HACD-TECR complex interface inhibits CRC cell growth. a,** Overall structure the *C. elegans* HACD subunit. **b,** A representative snapshot of the MD simulations at 24 ns

showing Y142 and E149 near the C-2 and C-3 positions of the 3-hydroxyacyl-CoA substrate. **c,** Functional characterization of the catalytic residues on HACD by the in vitro VLCFA elongation assay. The activities of HACD mutants were normalized relative to that of the WT. **d,** Detailed view of the *C. elegans* HACD-TECR binding interface. The hydrogen-bonds between HACD and TECR are shown by red dashed lines. The hydrogen-bonds formed within the U-shaped TM5/6 loop of HACD are indicated by black dashed lines. **e,** The M170 and N175 residues from the U-shaped TM5/6 loop of HACD insert into a small cavity of TECR. **f,** Mutation of the *C. elegans* HACD-TECR interface residues disrupts complex formation. His-tagged HACD and Flag-tagged TECR were co-expressed and co-immunoprecipitated for WB analysis. **g,** Mutation of the human equivalent HACD2-TECR interface residues disrupts complex formation. **h,** Disruption of the HACD-TECR interface suppress CRC cell proliferation. **i,** Western blot analysis of TECR expression. TECR WT or variants was expressed in **h**.

Data are representative of three independent experiments. Error bars are mean ± SD. ***P < 0.001, ****P < 0.0001 by one-way ANOVA multiple comparisons test; ns, not significant; asterisk shows comparison with wild-type (c) or control group (h).

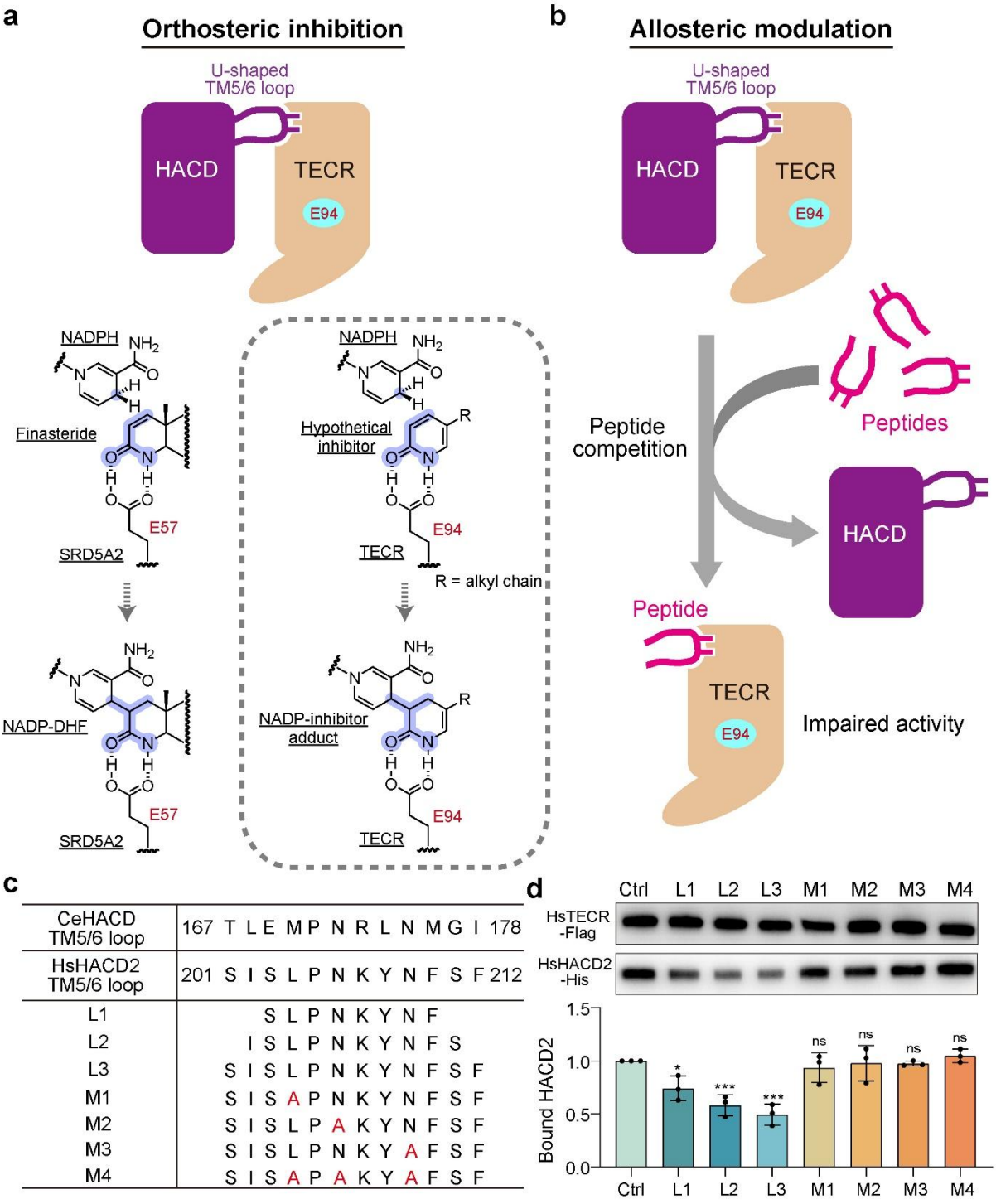

Fig. 7 | Orthosteric and allosteric strategies targeting TECR to modulate VLCFA biosynthesis.

a-b, Illustration of the orthosteric inhibition (**a**) and allosteric modulation (**b**) strategies targeting TECR.

Panel **a**: TECR orthosteric inhibitor design strategy inspired by the SRD5A2 inhibitor finasteride. The

NADP-dihydrofinasteride (NADP-DHF) adduct represents a potent inhibitor of SRD5A2. In SRD5A2,

742 catalytic residue E57 is essential for coordinating the amide group of finasteride, thereby enabling
743 NADPH-dependent reduction of the adjacent C=C bond to yield the NADP–DHF adduct. Analogously,
744 catalytic residue E94 in TECR could serve to coordinate an inhibitor featuring a nitrogen-containing
745 heterocycle and extended alkyl chains, thereby facilitating formation of a covalent NADP–inhibitor
746 adduct. Panel **b**: schematic diagram of an allosteric strategy to uncouple HACD2 and TECR through
747 peptide competition to impair TECR activity. **c,** A list of peptides designed based on the U-shaped
748 TM5/6 loop sequence of HACD to disrupt HACD-TECR interface. **d,** Competition efficiency analysis of
749 the peptides evaluated by WB analysis. Upper panel: a representative result of WB analysis. Lower
750 panel: quantification and statistical analysis of three independent WB results. Data are representative
751 of three independent experiments. Error bars are mean ± SD. *P < 0.05, ***P < 0.001 by one-way
752 ANOVA multiple comparisons test; ns, not significant; asterisk shows comparison with control group.

753

754